

Learning for Unconstrained Space-Time Video Super-Resolution

Zhihao Shi, Chengqi Li, Linhui Dai, Xiaohong Liu, *Graduate Student Member, IEEE*, Jun Chen, *Senior Member, IEEE*, Timothy N. Davidson, *Fellow, IEEE*

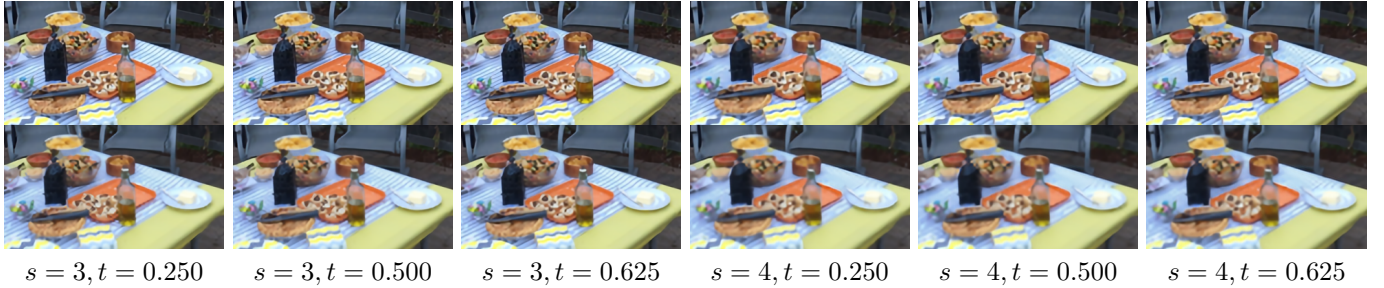


Fig. 1: Comparison between the proposed method (the first row) and a state-of-the-art two-stage method: BMBC [1] + Meta-SR [2] (the second row).

Abstract—Recent years have seen considerable research activities devoted to video enhancement that simultaneously increases temporal frame rate and spatial resolution. However, the existing methods either fail to explore the intrinsic relationship between temporal and spatial information or lack flexibility in the choice of final temporal/spatial resolution. In this work, we propose an unconstrained space-time video super-resolution network, which can effectively exploit space-time correlation to boost performance. Moreover, it has complete freedom in adjusting the temporal frame rate and spatial resolution through the use of the optical flow technique and a generalized pixelshuffle operation. Our extensive experiments demonstrate that the proposed method not only outperforms the state-of-the-art, but also requires far fewer parameters and less running time.

Index Terms—Unconstrained video super-resolution, generalized pixelshuffle layer.

I. INTRODUCTION

Video enhancement is a classical problem in computer vision. It consists of two major tasks: video frame interpolation (VFI) [3]–[11] and video super-resolution (VSR) [12]–[17], which aim to increase temporal frame rate and spatial resolution, respectively.

Space-time video super-resolution (STVSR), which attempts to accomplish VFI and VSR simultaneously, has received significant attention in recent years. The traditional approaches to STVSR [18]–[21] typically rely on strong assumptions or hand-crafted priors, and consequently are only suited to specific scenarios. The advent of deep learning has revolutionized many areas in computer vision and multimedia

signal processing, including, among others, image dehazing [22]–[24], salient object detection [25], [26], action recognition [27], [28], and video captioning [29], [30]. In particular, it enables the development of data-driven approaches to VFI and super-resolution (SR) [31]–[34] that can capitalize on the learning capability of neural networks as opposed to relying on prescribed rules. STVSR also naturally benefits from this advancement since it can be realized via a direct combination of VFI and SR. Specifically, one can first use VFI to increase the temporal frame rate, then leverage SR to enhance the spatial resolution. Moreover, the state-of-the-art (SOTA) VFI and SR methods (e.g., the flow-based VFI methods [3]–[8] and the meta-learning-based SR methods [2]) have the freedom to adjust the frame rate and the spatial resolution, respectively. As a consequence, the resulting two-stage scheme is able to perform unconstrained STVSR. However, as pointed out in [35], [36], this two-stage scheme does not take advantage of the intrinsic relationship between temporal and spatial information, which limits the highest resolution that can be potentially achieved (see Fig. 1). In addition, performing STVSR in a two-stage fashion tends to be highly inefficient since VFI and SR are computationally intensive by themselves and likely involve many operations that can be shared.

To tackle these problems, some recent works [35], [36] have proposed a one-stage approach to STVSR by consolidating VFI and SR. This boosts performance by a large margin, while involving far fewer parameters and incurring less computational cost. However, this gain comes at a price. Indeed, compared to its two-stage counterpart, the new approach in [35], [36] lacks flexibility in the choice of the final temporal/spatial resolution. Specifically, in the temporal domain, the convolution neural network (CNN) employed to synthesize the intermediate frame (based on two input frames) is tailored to a particular target time. As for the spatial domain, due to the use of the pixelshuffle layer [37] or deconvolution

Z. Shi, C. Li, L. Dai, X. Liu (corresponding author), J. Chen and T.N. Davidson are with the Department of Electrical and Computer Engineering, McMaster University, Hamilton, ON., L8S 4K1, Canada (e-mail: {shiz31, lic222, dai15, liux173, chenjun, davidson}@mcmaster.ca). This work was supported in part by the Natural Sciences and Engineering Research Council of Canada through a Discovery Grant.

layer, it is impossible to adjust the up-sampling factor without modifying or retraining the network. Besides, the intrinsic limitation of these two layers renders fractional up-sampling factors unrealizable.

A natural question that arises here is whether the performance of the one-stage scheme can be retained without compromising flexibility. We offer an affirmative answer in this work by proposing an Unconstrained Space-Time Video Super-Resolution Network (USTVSRNet), which is able to increase the temporal/spatial resolution of a given video by an arbitrary factor. For temporal interpolation, the optical flow technique is adopted to ensure the desired flexibility in the temporal resolution. Moreover, different from [35], [36], where the intermediate frame is synthesized at the feature level, we make predictions at both the image and feature levels, which leads to a noticeable performance improvement. As to spatial up-sampling, we introduce a Generalized Pixelshuffle Layer (GPL) that can project low-dimensional features to a high-dimensional space with the dimension ratio freely chosen. In addition, we construct a Scale-Attentive Residual Dense Block (SARDB) to generate scale-aware features. Due to the innovative features of our design, USTVSRNet is capable of up-sampling frames by an arbitrary factor with a single model. Our experimental results will show that the proposed method outperforms the SOTA two-stage methods, and does so with significantly lower computational cost.

The main contributions of this paper are as follows: (1) We propose a novel unconstrained STVSR method, which possesses the strengths of the SOTA one-stage and two-stage approaches while avoiding their drawbacks. (2) Several new mechanisms are introduced, including, integrating image-level and feature-level information to improve the quality of the synthesized intermediate frame, generalizing the standard pixelshuffle layer (SPL) to increase the degrees of freedom in terms of up-sampling factor, and generating scale-aware features to make the network more adaptive.

II. RELATED WORK

A. Video Frame Interpolation

The goal of VFI is to increase the frame rate by synthesizing intermediate frames while maintaining spatial and temporal consistencies with the given video frames. There are two major categories of video interpolation methods: kernel-based and flow-based methods.

As a pioneer of the kernel-based method, reference [10] employs a rigid spatially-adaptive convolution kernel to generate each target pixel. Naturally, very large kernels are needed for covering large motions, which leads to a substantial memory overhead. Reference [11] replaces regular 2D convolution kernels with pairs of 1D kernels to reduce the memory overhead. Even though that reduction is significant, the method cannot handle motions that are larger than the kernel size. To solve this problem, AdaCoF [9] breaks the rigid limitation of the regular convolution kernel and proposes a 2D deformable spatially-adaptive convolution scheme for VFI. Later, GDConvNet, introduced in [38], further exploited the degrees of freedom available in the three dimension of space-time, which improves the performance significantly. While

kernel-based methods show promise, the time-oblivious nature of the convolution kernels means that the temporal information in the intermediate frames needs to be built into kernel-based methods in the design phase and cannot be easily adjusted during implementation.

In contrast, flow-based methods [4]–[8] generate the value of each pixel in the target intermediate frame according to an associated optical flow. Specifically, they first use the input frames to estimate source optical flows with the help of an optical flow estimation network [39]–[42]. They then convert the source optical flows into the associated ones with respect to the intermediate time t . Finally, the input frames are warped to the target frame according to these optical flows. As such, these methods have the inherent ability to perform interpolation with respect to an arbitrary time. Flow-based methods [4]–[7] typically adopt a linear model to convert the source optical flows. Recently, a quadratic model was proposed in [8], and preliminary results suggest that it may be able to better estimate the optical flows by exploiting four consecutive frames. For simplicity, in the present paper we will focus on the linear model, which involves two consecutive frames. It is straightforward to extend our work to incorporate higher-order models.

B. Super Resolution

SR has two main branches: single image super-resolution (SISR) and video super-resolution, which aim at recovering a visually pleasing high-resolution image and video, respectively.

In terms of SISR, an end-to-end network which maps the interpolated low resolution (LR) images to high resolution (HR) ones was proposed in [43], and was enhanced by increasing network depth or stacking more complicated modules in [44]–[47]. However, all of these methods need to pre-compute an interpolated LR image before applying convolution neural network, which significantly increases the computational complexity. To avoid the inefficient pre-computing process, the deconvolution layer and standard pixelshuffle layer (SPL), proposed by [48] and [37] respectively, enable the networks to directly output HR images from LR images, which dramatically reduces the computational complexity, and contributes to recovery of more fine-grained details.

On the other hand, the deconvolution layer and SPL also make it possible for VSR networks [12], [14]–[16], [31] to output HR videos from LR ones directly. The processing pipeline of the SOTA VSR methods is roughly as follows: extract features from the reference frame and neighboring frames, then feed them (after proper alignment and fusion) into a reconstruction network to generate a super-resolved frame. By employing a deconvolution layer or an SPL in the reconstruction network, the SOTA VSR methods have been shown to generate satisfactory results in terms of efficiency and effectiveness on various datasets.

Although the SOTA SISR and VSR methods have performed satisfactorily on many datasets, they lack flexibility in adjusting the resolution of the final output. This is due to the intrinsic limitations of the deconvolution layer and the SPL.

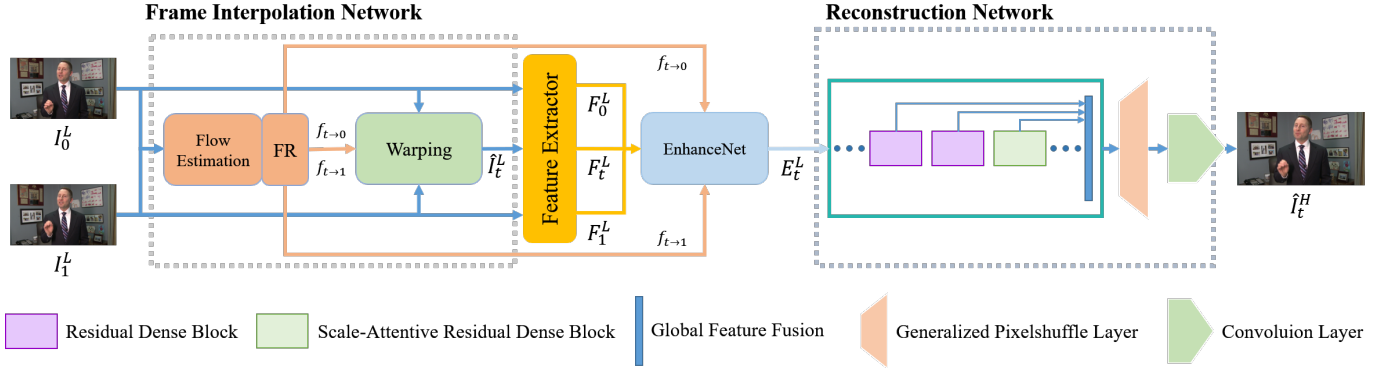


Fig. 2: Illustration of the architecture of USTVSRNet.

Recently, the meta-up-sample module proposed by [2] enables up-sampling by an arbitrary factor using a single model. Its refined version, known as the scale-aware up-sampling module [49], can better address the resulting memory overhead issues, but the underlying mechanism remains the same.

Unlike [2], [49], in the method proposed herein, we will generalize the SPL to release it from the constraints on the up-sampling factors. It will be shown that the new mechanism performs on par with, or slightly better than, SPL in terms of fixed scale up-sampling, and delivers better performance than that in [2], [49] in terms of up-sampling by arbitrary factors.

C. Space-Time Video Super-Resolution

Distinct from the separated operations of VFI and VSR, in a STVSR system we seek to simultaneously increase the temporal frame rate and the spatial resolution of a given video. This line of research was initiated in [50]. As the STVSR operation is a highly ill-posed inverse problem, due to the inadequacy of the available information, traditional methods [18]–[21] often resort to some hand-crafted priors or artificially-imposed constraints. For instance, reference [18] adopts a space-time directional smoothness prior and reference [19] makes a hypothesis that there is no great change in illumination for the static regions. As a result, these methods cannot cope with many real-world scenarios. In addition, the optimization for these methods is extremely computational inefficient (e.g., the processing speed for [19] is about 1 min/frame).

With the aid of deep learning, it is now possible to develop data-driven assumption-free STVSR methods. One simple way to do that is to realize STVSR via sequential execution of deep-learning-based VFI and SR. However, this two-stage scheme is suboptimal since it is susceptible to error accumulation and makes no use of space-time correlation. In addition, a direct combination of VFI and SR without any consolidation is clearly inefficient in terms of running cost.

In view of the problems with the two-stage approach, some one-stage STVSR methods [35], [36] have been proposed, which are able to offer improved performance at a reduced cost. While they are highly innovative, these newly-proposed methods [35], [36], have two major limitations. Firstly, due to the use of a CNN to directly synthesize the intermediate frames, the temporal position of such frames is not adjustable

after training. Secondly, there is no freedom to choose the spatial up-sampling factors to be different from those set in the training phase, nor to accommodate fractional factors. The main motivation of the present work is to remove these two limitations and realize unconstrained STVSR.

III. UNCONSTRAINED SPACE-TIME VIDEO SUPER-RESOLUTION NETWORK

The goal of the proposed USTVSRNet is to transform a low-resolution (LR) low-frame-rate (LFR) video into a high-resolution (HR) high-frame-rate (HFR) one. Specifically, given two LR input frames (I_0^L and I_1^L), an arbitrary target time $t \in [0, 1]$, and an arbitrary spatial up-sampling factor $s \in [1, +\infty)$, the goal is to synthesize an intermediate HR frame I_t^H with $H = sL$. The overall architecture of USTVSRNet is shown in Fig. 2, which mainly consists of 4 sub-networks: a Frame Interpolation Network (FINet), a Feature Extractor, an Enhancement Network (EnhanceNet), and a Reconstruction Network.

As illustrated in Fig. 2, first a LR intermediate frame \hat{I}_t^L is constructed by the FINet based on neighboring source frames (I_0^L and I_1^L) and bidirectional optical flows ($f_{t \rightarrow 0}$ and $f_{t \rightarrow 1}$). Then the features F_0^L , F_t^L and F_1^L are generated through the feature extractor from I_0^L , \hat{I}_t^L and I_1^L respectively. Next, F_t^L is enhanced to E_t^L at the feature level through the enhancement network, and, finally, E_t^L is fed into the reconstruction network to produce a high-resolution frame \hat{I}_t^H as an approximation of I_t^H . The details of each of these steps are outlined below.

A. Frame Interpolation Network

Given I_0^L and I_1^L , the FINet is employed to generate a coarse prediction \hat{I}_t^L as the reference frame, which will be used in conjunction with the feature-level prediction to produce the final reconstruction. In principle, any flow-based VFI algorithm can serve this purpose. However, the SOTA systems [4]–[6], [8] often involve complex designs (e.g., depth information [5], quadratic model [8]), and consequently are not very efficient as a component of a larger system. For this reason, we consider a simple design for the FINet.

First a light-weight optical flow estimation network (PWC-Net [42]) is utilized to estimate the bidirectional flows $f_{0 \rightarrow 1}$

and $f_{1 \rightarrow 0}$. They are then passed to the flow reverse layer [8] to predict backward flows $f_{t \rightarrow 0}$ and $f_{t \rightarrow 1}$. Specifically, we have

$$f_{t \rightarrow 0} = \text{FR}(f_{0 \rightarrow t}), \quad (1)$$

where $f_{0 \rightarrow t} = t * f_{0 \rightarrow 1}$, and FR denotes the flow reverse operation [8]; $f_{t \rightarrow 1}$ can be computed in a similar way. Finally the reference frame is synthesized as:

$$\hat{I}_t^L = \frac{(1-t) \cdot B \cdot g(I_0^L, f_{t \rightarrow 0}) + t \cdot (1-B) \cdot g(I_1^L, f_{t \rightarrow 1})}{(1-t) \cdot B + t \cdot (1-B)}, \quad (2)$$

where B is a blending mask generated by a small CNN [4], [8], [51], and $g(\cdot)$ denotes the warping function.

B. Feature Extractor

The frame features F_0^L , F_t^L and F_1^L are extracted from I_0^L , \hat{I}_t^L and I_1^L , respectively, through a feature extractor, which is composed of a convolution layer and several residual blocks [52].

C. Enhancement Network

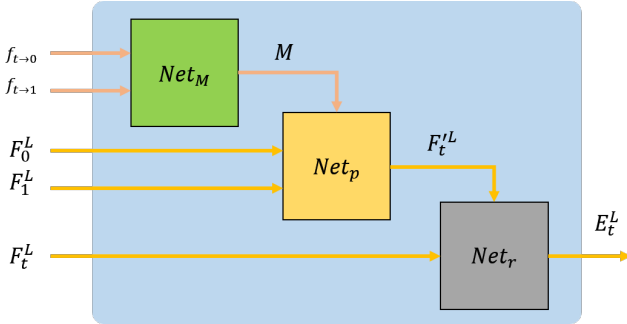


Fig. 3: Illustration of the architecture of EnhanceNet.

As illustrated in Fig. 3, the inputs to the enhancement network consist of the three extracted feature maps F_0^L , F_t^L , F_1^L as well as the pre-computed bidirectional optical flows $f_{t \rightarrow 0}$, $f_{t \rightarrow 1}$. The goal of this sub-network is threefold: 1) leverage the source frame features (F_0^L and F_1^L) and the bidirectional optical flows ($f_{t \rightarrow 0}$ and $f_{t \rightarrow 1}$) to predict the features of the intermediate frame $F_t'^L$; 2) refine the generated reference frame at the feature level to alleviate the error accumulation problem as the coarse prediction \hat{I}_t^L obtained in the first stage tends to have many artifacts; 3) fuse the source frames to the intermediate frame for better reconstruction under the guidance of $f_{t \rightarrow 0}$, $f_{t \rightarrow 1}$. The operation of the enhancement network can be expressed as:

$$M = \text{Net}_M(f_{t \rightarrow 0}, f_{t \rightarrow 1}), \quad (3)$$

$$F_t'^L = \text{Net}_p(F_0^L, F_1^L, M), \quad (4)$$

$$E_t^L = \text{Net}_r(F_t^L, F_t'^L), \quad (5)$$

where M denotes the motion features extracted from $f_{t \rightarrow 0}$ and $f_{t \rightarrow 1}$ through Net_M .

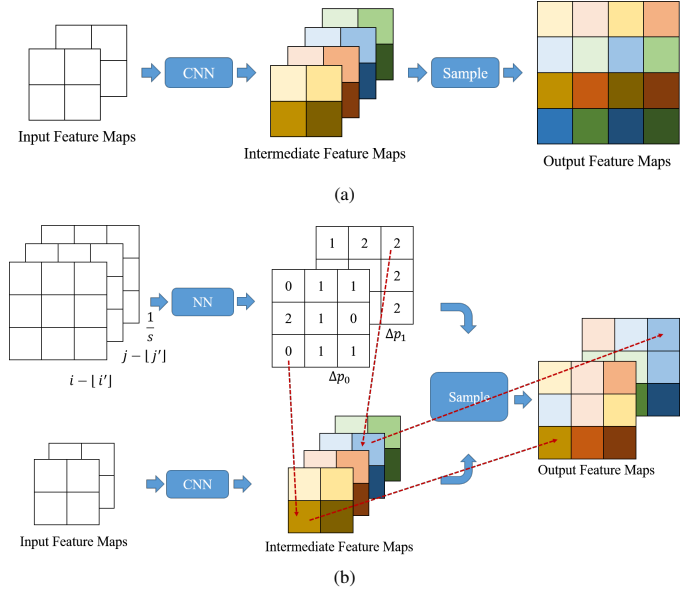


Fig. 4: Examples of the standard and generalized pixelshuffle layers, where (a) shows the standard layer while $C_{in} = 2, C_{int} = 4, C_{out} = 1$, and $s = 2$; (b) shows the generalized pixshuffle layer while $C_{in} = 2, C_{int} = 4, C_{out} = 2$, $s = 1.5$, and $p_c = 0$.

D. Reconstruction Network

The reconstruction network is designed using the residual dense network [47] as the backbone. We replace the SPL with a novel GPL described below, making it possible to up-sample low-resolution features by an arbitrary scale factor s . Moreover, we substitute one out of every K RDBs with our newly constructed SARDB, which is able to generate scale-adaptive features and contribute positively to the overall performance.

1) *Generalized Pixelshuffle Layer*: a new GPL is proposed to address the lack of flexibility in the SPL. Here we describe both the SPL and the GPL in parallel and highlight their differences.

The goal of the SPL and the GPL is to convert input feature maps of size $C_{in} \times H \times W$ to output feature maps of size $C_{out} \times sH \times sW$ for some scale factor s (s is allowed to be fractional for GPL but not for SPL). They both proceed in three steps:

Widen Input Features: The input feature maps are transformed via convolution to the intermediate feature maps T of size $C_{inter} \times H \times W$. Note that C_{inter} must be equal to $s^2 C_{out}$ for SPL, but can be an arbitrary positive integer for GPL.

Location Projection: Each spatial position on the output feature maps (i, j) , $i \in [0, sH-1]$, $j \in [0, sW-1]$ is projected to $(i', j') = (\frac{i}{s}, \frac{j}{s})$ on the intermediate feature maps.

Feature Mapping: Sample features from the intermediate feature maps T for each 3D output position (i, j, c) , $c \in [0, C_{out}-1]$ on the output feature maps according to a certain rule. Specifically, for SPL, the rule can be formulated as follows according to [37]:

$$\text{SPL}(T)_{i,j,c} = T_{\lfloor i' \rfloor, \lfloor j' \rfloor, C_{out} \cdot s \cdot \text{mod}(i,s) + C_{out} \cdot s \cdot \text{mod}(j,s) + c}. \quad (6)$$

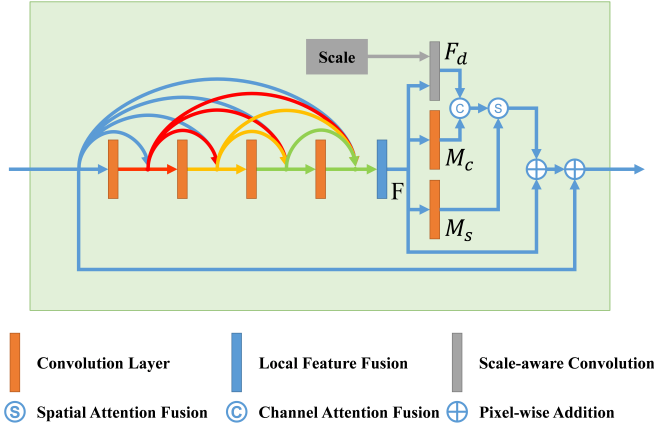


Fig. 5: Illustration of the SARDB architecture.

A concrete example can be found in Fig. 4 (a). In contrast, for GPL, we propose to sample using

$$\text{GPL}(T)_{i,j,c} = T_{\lfloor i' \rfloor, \lfloor j' \rfloor, p_c + \Delta p_c}, \quad (7)$$

where p_c is a pre-determined channel position and Δp_c denotes an adaptive offset predicted by a small fully connected network with $(i' - \lfloor i' \rfloor, j' - \lfloor j' \rfloor, 1/s)$ as input (which is inspired by [2]). Note that we associate each 3D output position with a Δp_c , resulting in $sH \cdot sW \cdot C_{\text{out}}$ offsets in total. In the case where $p_c + \Delta p_c$ is not an integer, the sampling value $T_{\lfloor i' \rfloor, \lfloor j' \rfloor, p_c + \Delta p_c}$ can be computed using a linear interpolation function:

$$T_{\lfloor i' \rfloor, \lfloor j' \rfloor, p_c + \Delta p_c} = \sum_{i=0}^{C_{\text{out}}-1} \max(0, 1 - |p_c + \Delta p_c - i|) \cdot T_{\lfloor i' \rfloor, \lfloor j' \rfloor, i}. \quad (8)$$

By designing so, the sampling position $(\lfloor i' \rfloor, \lfloor j' \rfloor, p_c + \Delta p_c)$ on the intermediate feature maps is capable of moving along the channel direction to sample the needed feature. We provide a concrete example in Fig. 4 (b)

From Eqs. (6)-(7) and Fig. 4, we have two observations: 1) the proposed GPL not only achieves unconstrained up-sampling of feature maps but also has the capability to freely specify the channel dimension of the intermediate feature maps; 2) the GPL degenerates to the SPL if we set $C_{\text{inter}} = s^2 C_{\text{out}}$, $p_c = C_{\text{out}} \cdot r \cdot \text{mod}(i, s) + C_{\text{out}} \cdot r \cdot \text{mod}(j, s) + c$, and force $\Delta p_c = 0$. From these two points, it can be seen that the proposed GPL is a generalized version of the SPL with more degrees of freedom that can be fruitfully explored.

In our implementation, we will choose $p_c = c \cdot \frac{C_{\text{inter}}}{C_{\text{out}}} + \frac{C_{\text{inter}}/C_{\text{out}}-1}{2}$, initialize $\Delta p_c = 0$, and set the learning rate of the small fully connected layer to be the same as the global learning rate.

2) *Scale-Attentive Residual Dense Block*: As pointed out in [49], the features generated by SR networks can be divided into scale-independent ones and scale-dependent ones, and the latter should be adapted to different scales. However, the scale-aware adaptation module introduced by [49] is built solely upon the spatial-wise attention mechanism, and makes no use of channel-wise attention [53]. With this observation, we propose SARDB to exploit the available degrees of freedom more thoroughly.

The architecture of the proposed SARDB is shown in Fig. 5. The features F output by the LFF [47] are fed into several convolution layers to generate spatial attention map M_s and channel attention map M_c respectively. Then, scale-aware convolution [49] is employed to convert the features F into scale-dependent features F_d , which are then modulated by M_s and M_c by broadcasting and multiplication. Finally, the results from the upper and lower branches are merged to produce scale-adaptive features.

IV. EXPERIMENTS FOR UNCONSTRAINED SPACE-TIME VIDEO SUPER-RESOLUTION

Unconstrained STVSR methods can flexibly adjust the temporal frame rate and the spatial resolution of the output video. In this section, we discuss the unconstrained STVSR. The experiment for fixed STVSR will be presented in Section V.

A. Implementation Details

In our experiments, we explore the performance for different values of the target time t and the up-sampling factor s . We let t vary from 0 to 1 with a step size of 0.125, and s vary from 1 to 4 with a step of 0.5. During the implementation, we set $K = 4$ and $C_{\text{inter}} = 5C_{\text{in}} = 5C_{\text{out}} = 5 \times 64$ respectively. The adopted loss function, training dataset, and training strategy are described below.

1) *Loss Function*: We employ two loss terms to train our network, being L_1 loss and perceptual loss [54], respectively: **L_1 Loss**: The L_1 loss is used to measure the difference between the prediction and the ground-truth in a per-pixel manner, and can be formulated as follows:

$$\mathcal{L}_1 = \sum_x \|\hat{I}_t^H(x) - I_t^H(x)\|_1. \quad (9)$$

The L_2 loss can also be used, but it is widely known in the image synthesis area that the L_2 loss could lead to blurry results to a certain degree. Following [9], [55], we adopt Charbonnier penalty function [56] to optimize L_1 loss function and set $\epsilon = 10^{-6}$.

Perceptual Loss: Different from the per-pixel loss, the perceptual loss seeks to measure the difference from a global visual view, which has been shown effective in generating visually realistic images. The perceptual loss often leverages multi-scale feature maps extracted from a pre-trained network to quantify the difference. Here, we adopt VGG-16 [57] as the pre-trained network, and use feature maps from the last layer of each of the first three stages to measure the difference (*i.e.*, Conv1_2, Conv2_2 and Conv3_3). The loss can be expressed in the following form:

$$\mathcal{L}_p = \sum_{i=1}^3 \|\Phi_i(\hat{I}_t^H) - \Phi_i(I_t^H)\|_2^2, \quad (10)$$

where $\Phi_i(I_t^H)$, $i = 1, 2, 3$ are the aforementioned three feature maps corresponding to I_t^H while $\Phi_i(\hat{I}_t^H)$ corresponds to \hat{I}_t^H . **Overall Loss**: By combining the L_1 loss and the perceptual loss, the overall loss can be defined as:

$$\mathcal{L} = \mathcal{L}_1 + \lambda \mathcal{L}_p, \quad (11)$$

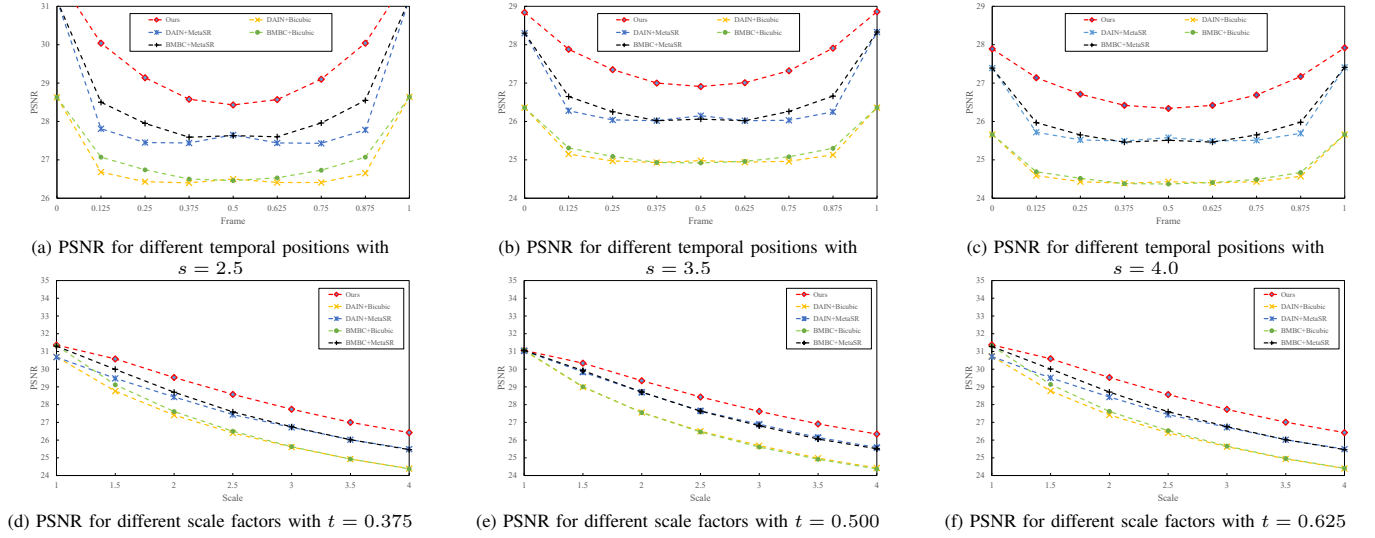


Fig. 6: Quantitative comparisons of unconstrained STVSR methods on Adobe240 dataset.

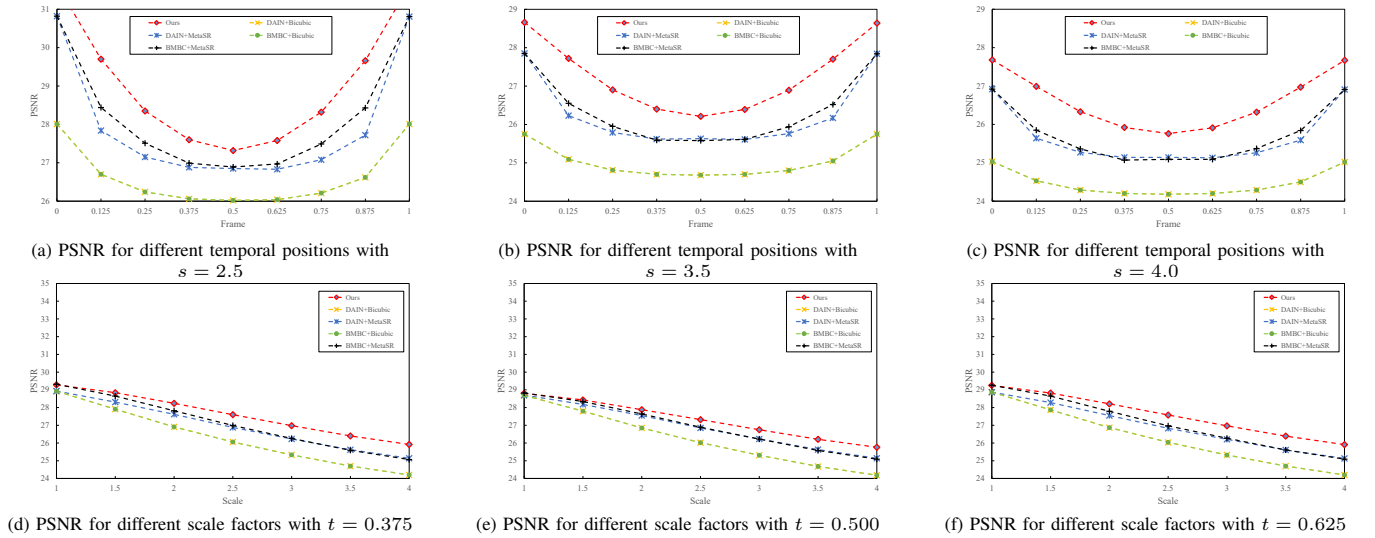


Fig. 7: Quantitative comparisons of unconstrained STVSR methods on Gopro dataset.

where λ is a hyper-parameter to balance the L_1 loss term and the perceptual loss term. Experimentally, we find setting $\lambda = 0.04$ reaches the best performance.

2) *Training Dataset*: Adobe-240 dataset [58] consists of 133 handheld recorded videos, which mainly contain outdoor scenes. The frame rate of each video is 240 fps, with spatial resolution as $720 \times 1,280$. From this set, 103 videos are randomly selected to construct our training dataset. That set is formed by successively grouping every 9 consecutive frames, and resizing them to 360×640 to form a training sequence $I_0^H, I_{0.125}^H, \dots, I_1^H$. In this way, we obtain 10,895 sequences in total. The LR frames are generated through bicubic down-sampling from the HR frames. We randomly crop image patches of size 56×56 from the LR frames for training. Horizontal/vertical flipping as well as temporal order reversal is performed for data augmentation.

3) *Training Strategy*: During the training phase, t and s are randomly selected to build each training batch. The image

patches within a single batch share the same t and s . We adopt the Adam optimizer [59] with a batch size of 18, where β_1 and β_2 are set to the default values 0.9 and 0.999, respectively. We train our network for 30 epochs in total with the initial learning rate set to 10^{-4} , and the learning rate is reduced by a factor of 10 at epoch 20. The training is carried out on two NVIDIA GTX 2080Ti GPUs, which takes about one day to converge.

B. Evaluation Dataset

1) *Adobe Testing Dataset* [58]: We treat the remaining 30 videos of the Adobe-240 dataset as an evaluation dataset. As in the case of the training dataset, we successively group every 9 consecutive frames (resized to 360×640), resulting in 2,560 test sequences. For each sequence, the LR frames are generated from the HR ones via bicubic down-sampling.

2) *Gopro Testing Dataset* [60]: This dataset contains 11 videos recorded by a hand-held camera. The frame rate of



Fig. 8: Qualitative comparisons of different Unconstrained STVSR algorithms.

each video is 240 fps, and the image resolution is $720 \times 1,280$. The dataset is released in image format with a total of 12,221 images. We successively group every 9 consecutive images as a test sequence. In this way, 1,355 test sequences are generated.

C. Comparisons to SOTA methods

To the best of our knowledge, there is no one-stage method of this kind in the literature. So we only consider two-stage methods composed of SOTA unconstrained VFI methods (BMBC [1] and DAIN [5]) and SOTA SISR methods (since the code of [49] is not publicly available, we choose to use MetaSR [2]). Here we set $t = 0, 0.125, \dots, 1$ and $s = 1, 1.5, \dots, 4$ respectively.

Fig. 6 and Fig. 7 show (a)-(c) PSNR scores for different temporal positions with $s = 2.5, 3.5, 4.0$, (d)-(f) PSNR scores

TABLE I: Model size and running time comparisons with $s = 4$, where the model size is reported in millions (M) and the running time is reported in second (s) per frame.

Method	#Parameters (M)	Runtime (s)
USTVSRNet	12	0.12
BMBC + Meta-SR	33	0.34
BMBC + Bicubic	11	0.21
DAIN+Meta-SR	46	0.35
DAIN+Bicubic	24	0.18

for different scale factors with $t = 0.375, 0.500, 0.625$, on the Adobe240 and Gopro testing datasets, respectively. More results can be found in the supplementary materials. According to the experimental results, we make two observations: 1) the usage of more advanced VFI or SR methods contribute to bet-

ter predicted results. For example, although BMBC+MetaSR and DAIN+MetaSR are both equipped with the same SR method, the former performs better than the latter due to the fact that BMBC is more advanced than DAIN; 2) compared to two-stage methods, the proposed method has better performance and is much more stable. This is due to the fact that the components of the two-stage methods work in isolation and cannot exploit the relationships between behavior in space and time.

Fig. 8 shows some qualitative comparisons with $t = 0.5$ and $s = 4$. It can be seen that the proposed method tends to generate more visually appealing results than the others. For instance, the proposed USTVSRNet yields sharper and clearer strips in the first row of Fig. 8; the leaves and the flower pattern generated by our method are much clearer than others in the second and the third rows, respectively.

Tab. I provides comparisons between the methods in terms of model size and running time. Since two-stage methods are a simple concatenation of the VFI and SR algorithms, they tend to be overweight and slow. In contrast, the proposed method is more compact and efficient. Specifically, compared to the best performing two-stage method, namely BMBC + Meta-SR, the proposed USTVSRNet only has about 1/4 of size and takes half time to reconstruct one frame.

D. Ablation Study

TABLE II: Quantitative results of ablation study regarding FInet and EnhanceNet with $s = 4$, where PSNR and SSIM scores are averaged over t .

Method	PSNR	SSIM
(a) USTVSRNet w/o FInet	26.52	0.7815
(b) USTVSRNet w/o EnhanceNet	25.88	0.7486
(c) Complete USTVSRNet	26.83	0.7945

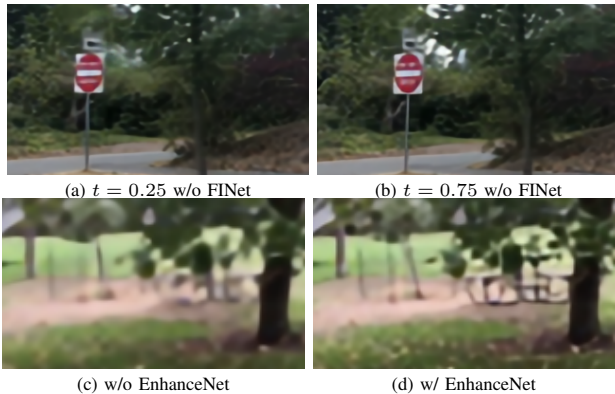


Fig. 9: Qualitative results of ablation study regarding FInet and EnhanceNet.

1) *Effectiveness of image-level and feature-level interpolation*: To validate the effectiveness of the image-level and feature-level interpolation, we consider the following three variants: 1) USTVSRNet without FInet (where the flow estimation and reverse network are still preserved to generate

optical flows for EnhanceNet). For this variant, we directly pass F_t^{L} to the reconstruction network; 2) USTVSRNet without EnhanceNet. For this variant, F_t^{L} is directly fed into the reconstruction network; 3) the complete network. We only provide the average scores over t with $s = 4$ in Tab. II due to paper space limitation. However, we observe similar results for different values of s .

From Tab. II (a) and (c), we can make the following two observations: 1) interpolating at the image level in addition to the feature level does contribute positively to the final reconstruction, leading to 0.31 dB improvement. It is expected that the performance can be improved further if more advanced VFI methods are adopted; 2) even without the explicit image-level prediction by FInet, the network still retains some, albeit reduced, ability to generate intermediate frames for different target times, owing to the implicit feature-level synthesis in EnhanceNet. A visual example is illustrated in Figs. 9 (a-b), in which two frames for different times are generated through USTVSRNet without FInet.

As can be seen from Tab. II (b-c), removing EnhanceNet degrades the performance by 0.85 dB in terms of PSNR. Indeed, in addition to the loss of feature-level interpolation, removing EnhanceNet deprives the system of the ability to refine the reference frame and gain information from the source frames for reconstruction, which leads to unsatisfactory results, as shown in Figs. 9 (c-d).

2) *Effectiveness of GPL and SARDB*: We next demonstrate the effectiveness of the GPL and SARDB. Since the reconstruction network is functionally orthogonal to the other three sub-networks, we repurpose it as an SISR network. The following experiments are based on the SISR network and the RDN [47] is adopted as the backbone. The Vimeo90K training and testing datasets are adopted. We first demonstrate the effectiveness of the GPL and then SARDB.

Comparison with SPL: As we stated in the previous section, the proposed GPL is a generalized version of the SPL. Here we compare them in terms of the fixed scale up-sampling. The baseline is RDN, which employs the SPL at the end of the network to upscale features by a fixed scale factor. We will denote this system by S-RDN. Then, we replace the SPL by the proposed GPL to obtain a system called G-RDN. We evaluate each method on up-sampling factors $r = 2, 3, 4$, respectively. For each scale factor, the baseline RDN needs to be modified and re-trained. In contrast, for G-RDN, we train it with a randomly selected scale factor $r \in [1, 4]$. To fairly compare, we also finetune G-RDN on each scale factor. However, we observe that finetuning operation leads to a relatively small increase in performance. The experiment results can be found in Tab. III.

As we can see from Tab. III, G-RDN achieves slightly better results than S-RDN at all scales with a negligible running time increase (except for $\times 4$ up-sampling on which G-RDN performs a little worse in terms of the SSIM value), which implies the performance of the GPL is on par or marginally better than that of the SPL in the scenario of fixed scale up-sampling. More importantly, compared to the SPL, the GPL enables the network to have the capability to perform unconstrained up-sampling task, instead of restricted to certain

TABLE III: Comparisons between SPL and GPL in terms of the fixed scale up-sampling on the Vimeo90k dataset.

Method	scale-factor	PSNR	SSIM	Runtime
S-RDN	$\times 2$	40.81	0.9780	0.13
G-RDN	$\times 2$	40.85	0.9780	0.15
S-RDN	$\times 3$	36.27	0.9465	0.07
G-RDN	$\times 3$	36.29	0.9467	0.09
S-RDN	$\times 4$	33.88	0.9162	0.05
G-RDN	$\times 4$	33.90	0.9161	0.07

specific scaling factors. Therefore, from these two aspects, the GPL can be considered as a generalized version of the SPL.

Comparison with unconstrained up-sampling methods: Different from constrained counterparts, unconstrained methods are able to upscale an image by an arbitrary factor within a single model. For this part, we compare the GPL with certain unconstrained up-sampling modules. Since only a few methods concentrate on arbitrary scale factor upsampling, we need to design several baseline systems. The following three baselines are taken into consideration: 1) the first baseline directly adopt the bicubic interpolation technique to up-sample images, denoted as Bicubic; 2) we first use a standard RDN to up-sample a image by k times (k is a fixed integer), then resize the up-sampled image to the desired size with bicubic interpolation, denoted as I-RDN($\times k$); 3) we replace the SPL of RDN with the bicubic interpolation method, which means that bicubic interpolation is used to upscale the feature maps, denoted as Bi-RDN. In addition, we also compare with the SOTA unconstrained up-sampling method, Meta-RDN [2], which is the same as Bi-RDN and G-RDN except for the final up-sampling module. Bi-RDN, Meta-RDN, and G-RDN are trained with the same unconstrained training strategy. Tab. IV shows the evaluation results, which are averaged over $s \in [1, 4]$.

TABLE IV: Comparisons for different unconstrained upscale methods on Vimeo90k dataset.

Method	PSNR	SSIM	Runtime
Bicubic	37.41	0.9282	0.02
I-RDN($\times 2$)	38.25	0.9548	0.16
I-RDN($\times 4$)	38.02	0.9578	0.17
Bi-RDN	40.37	0.9586	0.17
Meta-RDN	40.72	0.9578	0.20
G-RDN	40.90	0.9590	0.18

Tab. IV illustrates the effectiveness of the proposed GPL. It has a clear advantage over other methods in terms of PSNR and SSIM. In particular, GPL outperforms the SOTA up-sampling module, Meta-Upscale, by about 0.18 dB and has a faster running speed.

Importance of channel direction freedom: To illustrate the importance of channel direction freedom, we consider the following variant: we keep other components the same as G-RDN except for forcing $\Delta p_c = 0$, in which the sampling position cannot move along the channel direction. This system

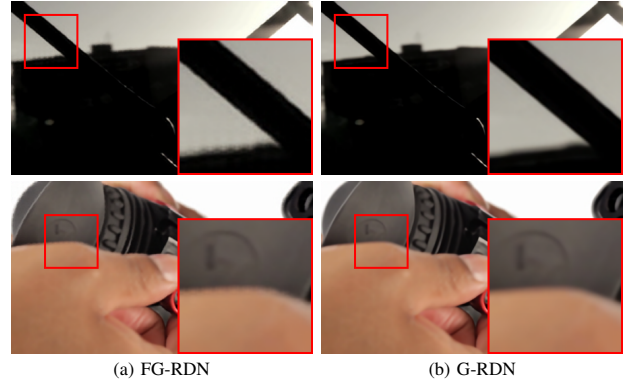


Fig. 10: Qualitative results of ablation study regarding channel dimension freedom.

TABLE V: Comparisons of FG-RDN and G-RDN with different C_{inter} .

Method	dimension	PSNR	SSIM	Runtime
FG-RDN	5×64	39.37	0.9525	0.17
G-RDN	1×64	40.78	0.9587	0.18
G-RDN	3×64	40.86	0.9589	0.18
G-RDN	5×64	40.90	0.9590	0.18
G-RDN	7×64	40.90	0.9590	0.18

is denoted by FG-RDN. The experimental results can be found in Tab. V, where one can easily find freedom of channel direction that leads to better reconstruction results. Indeed, if $\Delta p_c = 0$, then the local feature vectors of the output feature maps will become identical, which tends to generate blurry results or jagged edges. A visual example can be found in Fig. 10. Specifically, consider two different output positions on the output feature maps (i_1, j_1) and (i_2, j_2) . If they are projected to the same location on the intermediate feature maps $[i'_1], [j'_1] = [i'_2], [j'_2]$, their output feature vectors $\text{GPL}(T)_{i_1, j_1}$ and $\text{GPL}(T)_{i_2, j_2}$ will be exactly the same according to Eq. (7) (due to $\Delta p_c = 0$), which limits the diversity of the output feature maps. From another point of view, forcing $\Delta p_c = 0$ corresponds to using the nearest interpolation to up-sample the feature maps. Naturally, its performance is not as good as that of G-RDN, and it is even worse than Bi-RDN (since bicubic interpolation is superior to nearest interpolation in nature). Therefore, the channel direction freedom plays an important role in the GPL.

Choice of C_{inter} : For the all experiments above, we set $C_{\text{inter}} = 5C_{\text{in}} = 5C_{\text{out}} = 5 \times 64$. Now, we investigate how to choose the channel dimension of intermediate feature maps C_{inter} . We fix $C_{\text{in}} = C_{\text{out}} = 64$ and vary C_{inter} . Tab. V shows the results, which are averaged over $s \in [1, 4]$. As shown in Tab. V, as the dimension increases, the performance improves initially, but eventually becomes saturated. In particular, setting C_{inter} to more than 7×64 does not further improve the quality of the reconstructed HR image.

Effectiveness of SARDB: We finally investigate the contribution of the SARDB. Two networks are trained and evaluated on scale factor $r \in [1, 4]$: one with SARDB; the other one with RDB. We experimentally find that the scale-dependent

TABLE VI: Quantitative comparisons on Adobe240 dataset, Gopro dataset, and Vimeo90K dataset with $s = 4$, where ‘Center’ denotes the PSNR and SSIM value of the center frame $\hat{I}_{0.5}^H$ while ‘Whole’ is for average values of \hat{I}_0^H , $\hat{I}_{0.5}^H$, and \hat{I}_1^H . We highlight the first place and the second place in red and blue, respectively.

Method	#Parameters (million)	Adobe240		Gopro		Vimeo90k	
		Center	Whole	Center	Whole	Center	Whole
USTVSRNet	12	26.64/0.7944	27.43/0.8102	25.94/0.8093	26.91/0.8347	30.32/0.8866	31.20/0.8956
Zooming SloMo	11	26.36/0.7874	27.26/0.8069	25.84/0.8066	26.85/0.8333	30.11/0.8830	31.02/0.8928
STARNet	58	26.01/0.7639	27.01/0.7895	25.80/0.8053	26.80/0.8324	30.11/0.8828	30.92/0.8907
AdaCoF+RBPN	35	25.68/0.7501	26.64/0.7766	25.27/0.7773	26.25/0.8074	29.32/0.8612	30.48/0.8781
AdaCoF+DBPN	32	25.44/0.7322	26.46/0.7630	25.03/0.7612	26.01/0.7945	29.13/0.8543	30.30/0.8732
AdaCoF+Bicubic	22	24.27/0.6707	24.81/0.6910	24.10/0.7072	24.56/0.7278	27.36/0.8003	27.82/0.8122
BMBC+RBPN	24	25.73/0.7504	26.67/0.7767	25.29/0.7762	26.26/0.8069	29.36/0.8636	30.50/0.8793
BMBC+DBPN	32	25.51/0.7329	26.50/0.7633	25.07/0.7608	26.03/0.7643	29.28/0.8568	30.38/0.8745
BMBC+Bicubic	11	24.37/0.6696	24.86/0.6905	24.11/0.7057	24.56/0.7270	27.44/0.8023	27.86/0.8132

features generated by SARDB improve the performance by 0.28 dB and 0.0012 in terms of PSNR and SSIM, respectively, with negligible increasing in the running cost.

V. EXPERIMENTS FOR FIXED SPACE-TIME VIDEO SUPER-RESOLUTION

Different from unconstrained STVSR, in a fixed STVSR the temporal frame rate and the spatial resolution are not adjustable without retraining or modifying the network. Some experimental comparisons with the fixed STVSR are provided below.

A. Implementation Details

In this section, t can only vary among $\{0, 0.5, 1\}$ and s is set to 4, which means the network can only up-sample a video by $\times 2$ and $\times 4$ times in terms of temporal and spatial resolutions, respectively. As in the previous section, we set $K = 4$ and $C_{\text{inter}} = 5C_{\text{in}} = 5C_{\text{out}} = 5 \times 64$. The training dataset and training strategy are described below.

1) *Training Dataset*: The Vimeo90k Training Dataset [3] is adopted to train our model, where we have 51,312 sequences in total and the image resolution is 256×448 . Within each sequence, the first, the second and the third frames are treated as I_0^H , $I_{0.5}^H$ and I_1^H , respectively. Similarly, we use the bicubic down-sampling method to generate LR images from HR ones. We also perform horizontal and vertical flippings, as well as temporal order reversal, for data augmentation.

2) *Training Strategy*: For each training iteration, t is randomly selected from $\{0, 0.5, 1\}$ and s is set as 4 to construct the corresponding training batch. The Adam optimizer is adopted with a batch size of 24. We train the network for 25 epochs in total, with the initial learning rate as 10^{-4} . The learning rate is reduced by $\times 2$ times at every 8 epochs for the first 16 epochs and by $\times 5$ times every 3 epochs for the last 9 epochs. The training is carried out on two NVIDIA GTX 2080Ti GPUs, which takes about one day to converge.

B. Evaluation Dataset

1) *Adobe Testing Dataset and Gopro Testing Dataset*: The Adobe Testing Dataset and the Gopro Dataset from the previous section are directly used as the two evaluation

datasets for this section. There are 2,560 and 1,355 sequences in the Adobe dataset and the Gopro dataset, respectively, each with 9 frames. We only use the first, the fifth and the last frame of each sequence to compare different algorithms.

2) *Vimeo90k Testing Dataset* [3]: This dataset consists of 3,782 video sequences, each with 3 frames. The image resolution of this dataset is 256×448 . The first, second, and third frames in each video sequence are treated as I_0^H , $I_{0.5}^H$, and I_1^H respectively.

C. Comparisons to SOTA Methods

Here the Zooming SloMo [36] and STARNet [35] are chosen as representatives of one-stage fixed STVSR methods. For fair comparison, they are retrained on our training dataset using the same strategy. As to two-stage methods, we combine pre-trained SOTA VFI methods (AdaCoF [9] and BMBC [1]) and SR methods (RBPN [13] and DBPN [46] are chosen as representatives of the VSR and SISR methods, respectively).

We quantitatively compare our method with the chosen one-stage and two-stage methods under two well-known objective image quality metrics (PSNR and SSIM). The scores of the center frame and the average scores over all three frames are provided in Tab. VI. It can be seen that the proposed method ranks consistently at the top performance-wise, and comes in a close second in terms of the number of parameters. The two-stage methods not only suffer from large model size, but also lack competitiveness in performance since the constituent VFI and SR techniques are constrained to work in isolation. Although Zooming SloMo and STARNet are capable of handling diverse space-temporal patterns and improve the performance significantly, they are still behind the proposed method by a visible gap.

VI. CONCLUSION

In summary, we have proposed an unconstrained STVSR method that has the freedom to arbitrarily adjust the temporal frame rate and spatial resolution of the output video. Beyond using the optical flow technique for temporal interpolation, several new ideas are introduced, which include the generalized pixelshuffle operation for upsampling, a refined mechanism to generate scale-adaptive features, and the integration of image-level and feature-level representations. Despite their

excellent performance, it is conceivable that these new ideas could be further developed to yield even better performance. Moreover, there could well be likely alternative approaches to realizing unconstrained STVSR. In this sense, our work should be viewed as a stepping-stone towards a full-fledged framework for AI-enabled STVSR.

REFERENCES

- [1] J. Park, K. Ko, C. Lee, and C.-S. Kim, "BMBC: Bilateral motion estimation with bilateral cost volume for video interpolation," *arXiv preprint arXiv:2007.12622*, 2020.
- [2] X. Hu, H. Mu, X. Zhang, Z. Wang, T. Tan, and J. Sun, "Meta-SR: A magnification-arbitrary network for super-resolution," 2019.
- [3] T. Xue, B. Chen, J. Wu, D. Wei, and W. T. Freeman, "Video enhancement with task-oriented flow," *International Journal of Computer Vision*, vol. 127, no. 8, pp. 1106–1125, 2019.
- [4] W. Bao, W.-S. Lai, X. Zhang, Z. Gao, and M.-H. Yang, "MEMC-Net: Motion estimation and motion compensation driven neural network for video interpolation and enhancement," *IEEE Transactions on Pattern Analysis and Machine Intelligence*, 2019.
- [5] W. Bao, W.-S. Lai, C. Ma, X. Zhang, Z. Gao, and M.-H. Yang, "Depth-aware video frame interpolation," in *Proceedings of the IEEE Conference on Computer Vision and Pattern Recognition*, 2019, pp. 3703–3712.
- [6] H. Jiang, D. Sun, V. Jampani, M.-H. Yang, E. Learned-Miller, and J. Kautz, "Super slo-mo: High quality estimation of multiple intermediate frames for video interpolation," in *Proceedings of the IEEE Conference on Computer Vision and Pattern Recognition*, 2018, pp. 9000–9008.
- [7] S. Niklaus and F. Liu, "Context-aware synthesis for video frame interpolation," in *Proceedings of the IEEE Conference on Computer Vision and Pattern Recognition*, 2018, pp. 1701–1710.
- [8] X. Xu, L. Siyao, W. Sun, Q. Yin, and M.-H. Yang, "Quadratic video interpolation," in *Proceedings of the Advances in Neural Information Processing Systems*, 2019.
- [9] H. Lee, T. Kim, T.-y. Chung, D. Pak, Y. Ban, and S. Lee, "Adacof: Adaptive collaboration of flows for video frame interpolation," in *Proceedings of the IEEE Conference on Computer Vision and Pattern Recognition*, 2020, pp. 5316–5325.
- [10] S. Niklaus, L. Mai, and F. Liu, "Video frame interpolation via adaptive convolution," in *Proceedings of the IEEE Conference on Computer Vision and Pattern Recognition*, 2017, pp. 670–679.
- [11] —, "Video frame interpolation via adaptive separable convolution," in *Proceedings of the IEEE International Conference on Computer Vision*, 2017, pp. 261–270.
- [12] X. Wang, K. C. Chan, K. Yu, C. Dong, and C. Change Loy, "Edvr: Video restoration with enhanced deformable convolutional networks," in *Proceedings of the IEEE Conference on Computer Vision and Pattern Recognition Workshops*, 2019.
- [13] M. Haris, G. Shakhnarovich, and N. Ukita, "Recurrent back-projection network for video super-resolution," in *Proceedings of the IEEE Conference on Computer Vision and Pattern Recognition*, 2019, pp. 3897–3906.
- [14] P. Yi, Z. Wang, K. Jiang, J. Jiang, and J. Ma, "Progressive fusion video super-resolution network via exploiting non-local spatio-temporal correlations," in *Proceedings of the IEEE International Conference on Computer Vision*, 2019, pp. 3106–3115.
- [15] Y. Tian, Y. Zhang, Y. Fu, and C. Xu, "Tdan: Temporally-deformable alignment network for video super-resolution," in *Proceedings of the IEEE Conference on Computer Vision and Pattern Recognition*, 2020, pp. 3360–3369.
- [16] T. Isobe, S. Li, X. Jia, S. Yuan, G. Slabaugh, C. Xu, Y.-L. Li, S. Wang, and Q. Tian, "Video super-resolution with temporal group attention," in *Proceedings of the IEEE Conference on Computer Vision and Pattern Recognition*, 2020, pp. 8008–8017.
- [17] X. Liu, K. Shi, Z. Wang, and J. Chen, "Exploit camera raw data for video super-resolution via hidden markov model inference," *IEEE Transactions on Image Processing*, vol. 30, pp. 2127–2140, 2021.
- [18] E. Shechtman, Y. Caspi, and M. Irani, "Space-time super-resolution," *IEEE Transactions on Pattern Analysis and Machine Intelligence*, vol. 27, no. 4, pp. 531–545, 2005.
- [19] U. Mudanagudi, S. Banerjee, and P. K. Kalra, "Space-time super-resolution using graph-cut optimization," *IEEE Transactions on Pattern Analysis and Machine Intelligence*, vol. 33, no. 5, pp. 995–1008, 2010.
- [20] H. Takeda, P. Van Beek, and P. Milanfar, "Spatiotemporal video upscaling using motion-assisted steering kernel (mask) regression," in *High-Quality Visual Experience*. Springer, 2010, pp. 245–274.
- [21] O. Shahar, A. Faktor, and M. Irani, "Space-time super-resolution from a single video," in *Proceedings of the IEEE Conference on Computer Vision and Pattern Recognition*, 2011, pp. 3353–3360.
- [22] Y. Song, J. Li, X. Wang, and X. Chen, "Single image dehazing using ranking convolutional neural network," *IEEE Transactions on Multimedia*, vol. 20, no. 6, pp. 1548–1560, 2017.
- [23] C. Li, C. Guo, J. Guo, P. Han, H. Fu, and R. Cong, "PDR-Net: Perception-inspired single image dehazing network with refinement," *IEEE Transactions on Multimedia*, vol. 22, no. 3, pp. 704–716, 2019.
- [24] X. Liu, Y. Ma, Z. Shi, and J. Chen, "Griddehazenet: Attention-based multi-scale network for image dehazing," in *Proceedings of the IEEE International Conference on Computer Vision*, 2019, pp. 7314–7323.
- [25] S. Song, Z. Miao, H. Yu, J. Fang, K. Zheng, C. Ma, and S. Wang, "Deep domain adaptation based multi-spectral salient object detection," *IEEE Transactions on Multimedia*, 2020.
- [26] Z. Wu, S. Li, C. Chen, A. Hao, and H. Qin, "A deeper look at image salient object detection: Bi-stream network with a small training dataset," *IEEE Transactions on Multimedia*, 2020.
- [27] K. Zhu, R. Wang, Q. Zhao, J. Cheng, and D. Tao, "A cuboid cnn model with an attention mechanism for skeleton-based action recognition," *IEEE Transactions on Multimedia*, 2019.
- [28] T. Yu, L. Wang, C. Da, H. Gu, S. Xiang, and C. Pan, "Weakly semantic guided action recognition," *IEEE Transactions on Multimedia*, vol. 21, no. 10, pp. 2504–2517, 2019.
- [29] J. Wu, T. Chen, H. Wu, Z. Yang, G. Luo, and L. Lin, "Fine-grained image captioning with global-local discriminative objective," *IEEE Transactions on Multimedia*, 2020.
- [30] N. Xu, H. Zhang, A.-A. Liu, W. Nie, Y. Su, J. Nie, and Y. Zhang, "Multi-level policy and reward-based deep reinforcement learning framework for image captioning," *IEEE Transactions on Multimedia*, vol. 22, no. 5, pp. 1372–1383, 2019.
- [31] X. Yang, H. Mei, J. Zhang, K. Xu, B. Yin, Q. Zhang, and X. Wei, "DRFN: Deep recurrent fusion network for single-image super-resolution with large factors," *IEEE Transactions on Multimedia*, vol. 21, no. 2, pp. 328–337, 2018.
- [32] Z. He, Y. Cao, L. Du, B. Xu, J. Yang, Y. Cao, S. Tang, and Y. Zhuang, "MRFN: Multi-receptive-field network for fast and accurate single image super-resolution," *IEEE Transactions on Multimedia*, vol. 22, no. 4, pp. 1042–1054, 2019.
- [33] C. Tian, Y. Xu, W. Zuo, B. Zhang, L. Fei, and C.-W. Lin, "Coarse-to-fine cnn for image super-resolution," *IEEE Transactions on Multimedia*, 2020.
- [34] X. Zhang, P. Gao, S. Liu, K. Zhao, G. Li, L. Yin, and C. W. Chen, "Accurate and efficient image super-resolution via global-local adjusting dense network," *IEEE Transactions on Multimedia*, 2020.
- [35] M. Haris, G. Shakhnarovich, and N. Ukita, "Space-time-aware multi-resolution video enhancement," in *Proceedings of the IEEE Conference on Computer Vision and Pattern Recognition*, 2020, pp. 2859–2868.
- [36] X. Xiang, Y. Tian, Y. Zhang, Y. Fu, J. P. Allebach, and C. Xu, "Zooming slow-mo: Fast and accurate one-stage space-time video super-resolution," in *Proceedings of the IEEE Conference on Computer Vision and Pattern Recognition*, 2020, pp. 3370–3379.
- [37] W. Shi, J. Caballero, F. Huszar, J. Totz, A. P. Aitken, R. Bishop, D. Rueckert, and Z. Wang, "Real-time single image and video super-resolution using an efficient sub-pixel convolutional neural network," in *Proceedings of the IEEE Conference on Computer Vision and Pattern Recognition*, 2016, pp. 1874–1883.
- [38] Z. Shi, X. Liu, K. Shi, L. Dai, and J. Chen, "Video interpolation via generalized deformable convolution," *arXiv preprint arXiv:2008.10680*, 2020.
- [39] A. Dosovitskiy, P. Fischer, E. Ilg, P. Hausser, C. Hazirbas, V. Golkov, P. Van Der Smagt, D. Cremers, and T. Brox, "FlowNet: Learning optical flow with convolutional networks," in *Proceedings of the IEEE International Conference on Computer Vision*, 2015, pp. 2758–2766.
- [40] A. Ranjan and M. J. Black, "Optical flow estimation using a spatial pyramid network," in *Proceedings of the IEEE Conference on Computer Vision and Pattern Recognition*, 2017, pp. 4161–4170.
- [41] E. Ilg, N. Mayer, T. Saikia, M. Keuper, A. Dosovitskiy, and T. Brox, "FlowNet 2.0: Evolution of optical flow estimation with deep networks," in *Proceedings of the IEEE Conference on Computer Vision and Pattern Recognition*, 2017, pp. 2462–2470.
- [42] D. Sun, X. Yang, M.-Y. Liu, and J. Kautz, "PWC-Net: Cnns for optical flow using pyramid, warping, and cost volume," in *Proceedings of the IEEE Conference on Computer Vision and Pattern Recognition*, 2018, pp. 8934–8943.

- [43] C. Dong, C. C. Loy, K. He, and X. Tang, "Learning a deep convolutional network for image super-resolution," in *European Conference on Computer Vision*. Springer, 2014, pp. 184–199.
- [44] J. Kim, J. Kwon Lee, and K. Mu Lee, "Accurate image super-resolution using very deep convolutional networks," in *Proceedings of the IEEE Conference on Computer Vision and Pattern Recognition*, 2016, pp. 1646–1654.
- [45] K. Zhang, W. Zuo, S. Gu, and L. Zhang, "Learning deep cnn denoiser prior for image restoration," in *Proceedings of the IEEE Conference on Computer Vision and Pattern Recognition*, 2017, pp. 3929–3938.
- [46] M. Haris, G. Shakhnarovich, and N. Ukita, "Deep back-projection networks for super-resolution," in *Proceedings of the IEEE Conference on Computer Vision and Pattern Recognition*, 2018, pp. 1664–1673.
- [47] Y. Zhang, Y. Tian, Y. Kong, B. Zhong, and Y. Fu, "Residual dense network for image super-resolution," in *Proceedings of the IEEE Conference on Computer Vision and Pattern Recognition*, 2018, pp. 2472–2481.
- [48] C. Dong, C. C. Loy, and X. Tang, "Accelerating the super-resolution convolutional neural network," in *European Conference on Computer Vision*. Springer, 2016, pp. 391–407.
- [49] L. Wang, Y. Wang, Z. Lin, J. Yang, W. An, and Y. Guo, "Learning for scale-arbitrary super-resolution from scale-specific networks," *arXiv preprint arXiv:2004.03791*, 2020.
- [50] E. Shechtman, Y. Caspi, and M. Irani, "Increasing space-time resolution in video," in *Proceedings of the European Conference on Computer Vision*, 2002, pp. 753–768.
- [51] Z. Chi, R. M. Nasiri, Z. Liu, J. Lu, J. Tang, and K. N. Plataniotis, "All at once: Temporally adaptive multi-frame interpolation with advanced motion modeling," in *Proceedings of the European Conference on Computer Vision*, 2020.
- [52] K. He, X. Zhang, S. Ren, and J. Sun, "Deep residual learning for image recognition," in *Proceedings of the IEEE Conference on Computer Vision and Pattern Recognition*, 2016, pp. 770–778.
- [53] S. Woo, J. Park, J.-Y. Lee, and I. So Kweon, "CBAM: Convolutional block attention module," in *Proceedings of the European Conference on Computer Vision*, 2018, pp. 3–19.
- [54] J. Johnson, A. Alahi, and L. Fei-Fei, "Perceptual losses for real-time style transfer and super-resolution," in *European Conference on Computer Vision*. Springer, 2016, pp. 694–711.
- [55] Z. Liu, R. A. Yeh, X. Tang, Y. Liu, and A. Agarwala, "Video frame synthesis using deep voxel flow," in *Proceedings of the IEEE International Conference on Computer Vision*, 2017, pp. 4463–4471.
- [56] P. Charbonnier, L. Blanc-Feraud, G. Aubert, and M. Barlaud, "Two deterministic half-quadratic regularization algorithms for computed imaging," in *Proceedings of the IEEE International Conference on Image Processing*, vol. 2, 1994, pp. 168–172.
- [57] K. Simonyan and A. Zisserman, "Very deep convolutional networks for large-scale image recognition," in *Proceedings of the International Conference on Learning Representations*, 2014.
- [58] S. Su, M. Delbracio, J. Wang, G. Sapiro, W. Heidrich, and O. Wang, "Deep video deblurring for hand-held cameras," in *Proceedings of the IEEE Conference on Computer Vision and Pattern Recognition*, 2017, pp. 1279–1288.
- [59] D. P. Kingma and J. Ba, "Adam: A method for stochastic optimization," in *Proceedings of the 3rd International Conference on Learning Representations*, 2014.
- [60] S. Nah, T. Hyun Kim, and K. Mu Lee, "Deep multi-scale convolutional neural network for dynamic scene deblurring," in *Proceedings of the IEEE Conference on Computer Vision and Pattern Recognition*, 2017, pp. 3883–3891.